Article

Observation of quantum effects on radiation reaction in strong fields

Eva E. Los [1] ✉, Elias Gerstmayr [1,2,3], Christopher Arran [4],
Matthew J. V. Streeter [2], Cary Colgan [1,5], Claudia C. Cobo[1,4],
Brendan Kettle [1], Thomas G. Blackburn [6], Nicolas Bourgeois[7], Luke Calvin[2],
Jason Cardarelli[8], Niall Cavanagh[2], Stephen J. D. Dann [7],
Antonino Di Piazza [9,10,11], Rebecca Fitzgarrald [8], Anton Ilderton[12],
Christoph H. Keitel [11], Mattias Marklund[6,13], Paul McKenna [14],
Christopher D. Murphy [4], Zulfikar Najmudin [1], Peter Parsons[2,7],
Paramel Pattathil Rajeev [7], Daniel R. Symes[7], Matteo Tamburini [11],
Alexander G. R. Thomas [8], Jonathan C. Wood [1,15], Matthew Zepf[16,17,18],
Gianluca Sarri [2], Christopher P. Ridgers[4] & Stuart P. D. Mangles [1]

Radiation reaction, the force experienced by an accelerated charge due to radiation emission, has long been the subject of extensive theoretical and experimental research. Experimental verification of a quantum, strong-field description of radiation reaction is fundamentally important, and has wide-ranging implications for astrophysics, laser-driven particle acceleration, next-generation particle colliders and inverse-Compton photon sources for medical and industrial applications. However, the difficulty of accessing regimes where strong field and quantum effects dominate inhibited previous efforts to observe quantum radiation reaction in charged particle dynamics with high significance. We report a high significance (> 5σ) observation of strong-field radiation reaction on electron spectra where quantum effects are substantial. We obtain quantitative, strong evidence favouring the quantum-continuous and quantum-stochastic models over the classical model; the quantum models perform comparably. The lower electron energy losses predicted by the quantum models account for their improved performance. Model comparison was performed using a novel Bayesian framework, which has widespread utility for laser-particle collision experiments, including those utilising conventional accelerators, where some collision parameters cannot be measured directly.

Quantum effects dominate charge dynamics and radiation production[1,2] for charges accelerated by fields with strengths approaching the Schwinger field, $E_{sch} = 1.3 \times 10^{18}$ Vm^{-1}[3]. Such fields exist in extreme astrophysical environments, such as pulsar magnetospheres[4], may be accessed by high-power laser systems[5–7], dense particle beams interacting with plasma[8], crystals[9] and at the interaction point of next-generation particle colliders[10]. Radiation reaction affects the energy of inverse Compton scattered (ICS) photons used for various applications[11–17].

Classical radiation reaction theories do not limit the frequency of radiation emitted by accelerating charges and omit stochastic effects inherent in photon emission[18], thus demanding a quantum treatment.

Two quantum radiation reaction models, the quantum-continuous[19] and quantum-stochastic[2,20,21] models, correct the former issue, while only the quantum-stochastic model incorporates stochasticity[19]. Such models are of fundamental importance, providing insight into the effect of the electron self-force on its dynamics in electromagnetic fields.

In astrophysics, radiation reaction is predicted to limit electron-positron cascades, which populate the magnetospheres of pulsars, magnetars and active black holes with plasma[4,22] and can strongly affect reconnection in such plasmas[23,24]. Radiation reaction has been proposed as a dominant factor in gamma-burst generation[25] and is expected to influence the dynamics of pair plasmas[26], including relativistic current sheets[27]. Strong-field quantum radiation reaction may substantially affect the interaction point at high luminosity >100 GeV class particle colliders[10]. Strong electromagnetic fields produced by multi-petawatt laser systems[5–7,28,29] will enable the exploration of compact particle acceleration[30,31] and radiation generation[32] (e.g. via inelastic electron-photon scattering, termed Compton scattering[33]) in higher-power regimes.

In strong-field environments, quantum radiation reaction is expected to dominate laser-solid target interactions[34,35], ion-acceleration[36] and inverse Compton scattering (ICS), which has recently garnered considerable interest as a means of probing strong-field quantum electrodynamics[37,38].

Understanding the effect of radiation reaction on ICS photon spectra is crucial for diverse applications, including industrial, defence, archaeological[11,12] and medical[13] imaging, nuclear physics[14–16] and proposed schemes for gamma-gamma colliders[17].

The impact of radiation reaction on particle dynamics is characterised by the dimensionless intensity parameter, $a_0 = \frac{E_L e}{\omega_L m_e c}$ and the electron quantum parameter, $\eta = E_{RF}/E_{sch}$, where e and m_e are the magnitude of the electron charge and electron mass respectively, c is the speed of light in vacuum, E_L, E_{RF} are the external electric field (laser) strengths in the laboratory and electron rest frames, respectively, and ω_L is the electric field frequency in the laboratory frame. When $a_0 \gtrsim 1$, both relativistic and multi-(laser) photon effects become important. The regime of strong classical radiation reaction is characterised by $\alpha a_0 \eta \simeq 1$ and $\eta \ll 1$, where α is the fine structure constant[2,39]. Quantum effects dominate when $\alpha a_0 \simeq 1$ and $\eta \gtrsim 1$[2,39].

In regimes dominated by classical radiation reaction, an electron emits many photons, which each remove a small fraction of its energy[2,21,40]; radiation emission is treated as continuous and its impact on electron motion is well-described by the classical Landau-Lifshitz equation[18]. In the strong-field quantum regime, interactions with the laser field must be treated non-perturbatively and are absorbed into electron basis states by quantising the Dirac field in the presence of the laser field (Furry picture). Photon emission is described perturbatively with respect to these states[12] and becomes stochastic, with single emissions removing significant fractions of the electron energy[2]. In this work, the 'quantum-stochastic' model of radiation reaction employs the locally constant field approximation, which assumes emission events are point-like, depending only on local electric and magnetic fields, which are assumed to be constant over the timescale of photon emission[3]. Between emission events, electron motion is assumed to be classical, which is a good approximation in the ultra-relativistic regime[41].

The quantum-continuous model, known as the semi-classical model in the literature, aims to incorporate quantum physics in a classical framework, treating radiation emission as continuous[42], but capturing the same rate of change of average electron momentum as the quantum-stochastic model via the inclusion of a correction term, the Gaunt factor[19].

To date, six studies[9,43–46] have aimed to measure radiation reaction in strong fields ($a_0 \gg 1$). Of these studies, only one[44] conducted a quantitative comparison of different radiation reaction models, which was limited to 1σ significance.

Using an all-optical setup, we accessed $a_0 \approx 10$ and $\eta \lesssim 0.09$, for which strong-field non-perturbative effects dominate and quantum effects are influential, in contrast to early experiments at LINACs[47–49] and storage rings[50], for which $a_0 < 1$. Previous experiments at CORELS[45], ELI-NP and APOLLON[46], or using crystals[9,51,52], did not report an observation of radiation reaction on lepton spectra.

This work exceeds the 5σ significance threshold required for a definitive observation of radiation reaction and presents strong, quantitative evidence favouring quantum models over a classical model. This represents a substantial improvement on previous all-optical experiments, which reported $\leq 3\sigma$ evidence of radiation reaction and performed model selection with $< 1\sigma$ significance due to data scarcity and large uncertainties[43,44]. The higher significance of our findings is largely due to the greater number of successful collisions reported in this work (> 600) compared to previous all-optical experiments (< 10). This substantial increase in the number of successful collisions was enabled by the implementation of automated timing and pointing stabilisation of the laser.

Notably, our findings clarify outstanding questions raised by previous experiments[43,44] regarding the relative validity of different radiation reaction models in the classical-quantum regime.

The experimental setup is illustrated in Fig. 1a. Electron beams with mean energy ($609 \pm 2(stat)(12)(syst)$) MeV and a shot-to-shot standard deviation (40 ± 1) MeV (standard errors were calculated using bootstrapping due to non-normal data distributions), generated using laser-driven wakefield acceleration[31], collided with a tightly focused, counter-propagating laser pulse with $I = (1.0 \pm 0.2) \times 10^{21}$ W cm^{-2}, $\lambda_L = 2\pi c/\omega_L = 0.8$ μm, $a_0 = 21.4 \pm 1.8$ and $\langle \eta \rangle \leq 0.13 \pm 0.02$ at the laser focus, sufficient to probe the strong-field quantum regime. For more details, see 'experimental methods'.

Figure 1b compares predictions of post-collision electron and photon spectra for the classical, quantum-continuous and quantum-stochastic models. All models predict net electron energy losses (evidenced by lower-energy post-collision electron spectra), which, together with photon yield, scale with increasing a_0. These model-independent indicators of radiation reaction are used in the frequentist analysis in section 'Results and discussions'.

Quantum models prohibit the emission of photons with energies exceeding the electron energy, thus predicting lower energy losses than the classical model, evidenced by the mean post-collision electron energies and photon yields above 100 MeV in Fig. 1b). Unlike the classical and quantum-continuous models, the quantum-stochastic model predicts spectral broadening, arising from probabilistic photon emission[42,53,54], indicated by the relative widths of post-collision electron spectra in Fig. 1b.

The model-independent trends in Fig. 1b appear qualitatively in experimental data in Fig. 1c; this is purely illustrative and does not represent the frequentist analysis. In Fig. 1c, electron spectra for hits with moderate and high photon yields exhibit less pronounced high-energy peaks than randomly selected nulls, consistent with fewer high-energy electrons. As photon yield increases, the proportion of charge at high energies decreases.

Results and discussions

In lieu of measured pre-collision electron spectra, electron beams measured for misses and beam-off shots (nulls) are compared to those measured for successful collisions (hits). Hit and null identification is illustrated in Fig. 2a and discussed in the section 'Methods for frequentist analysis'. The profile screen background subtraction is detailed by Los[55].

Figure 2b illustrates two model-independent signatures of radiation reaction, identified by extensive simulation work provided in Supplementary Fig. 11 in Supplementary Information A.3 and as shown by Los et al.[56]. These are used to quantitatively examine whether differences between hits and nulls exceeded shot-to-shot
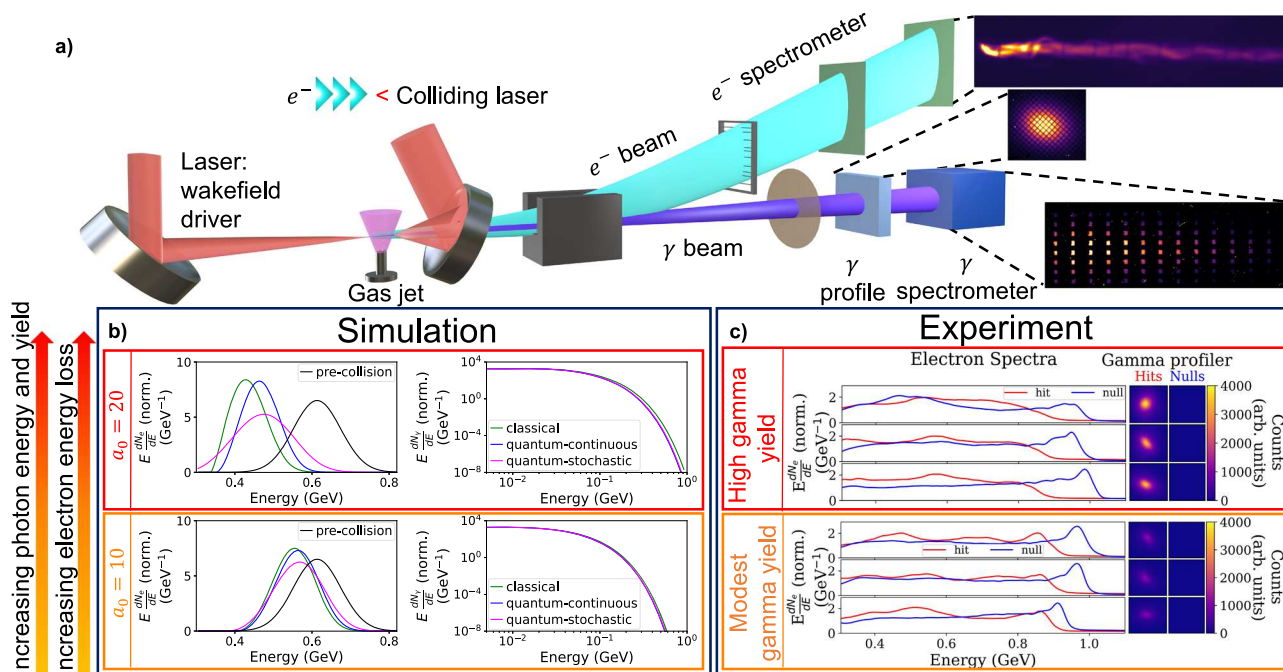
Fig. 1 | Experimental set-up, qualitative comparisons of measured hits and nulls and simulated radiation reaction models. a Experimental setup: one laser pulse, focused into a gas jet, drove a wakefield, accelerating electrons. A second, tightly focused, counter-propagating laser pulse collided with the electron beam, which emitted gamma photons. The electron spectrometer consisted of a dipole magnet, which dispersed the electron beam through a wire array onto two LANEX scintillating screens (green). A caesium iodide (CsI) profile screen and stack characterised the transverse profile and spectrum of the emitted gamma radiation, respectively. **b** Simulated post-collision electron spectra (normalised by integration) and photon spectra illustrating the classical, quantum-stochastic and quantum-continuous model predictions for $a_0 = 10$ (bottom) and $a_0 = 20$ (top). The electron beam and laser pulse collided 40 fs after the laser focus. The transverse and longitudinal laser intensity profiles were Gaussian, with respective full-width half-maxima (FWHM) of 2.47 μm and 30 fs. **c** Measured electron spectra for hits with high gamma profile yields are shown above those measured for and moderate yields, together with corresponding gamma profile signals. Nulls have been randomly selected.
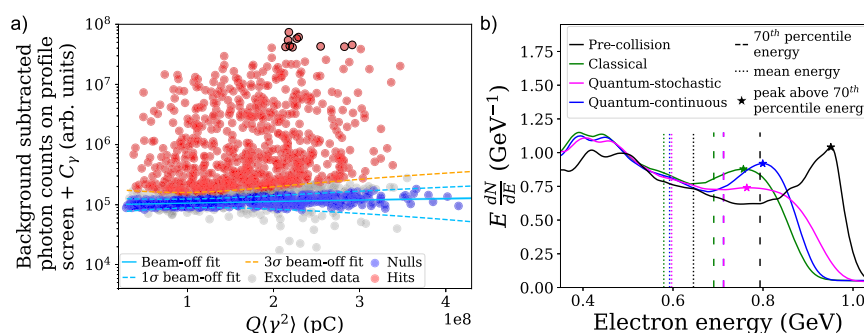

Fig. 2 | Shot selection and summary statistics. a The shot selection procedure is illustrated. Background-subtracted total counts measured by the gamma profile diagnostic are shown as a function of $Q\langle\gamma^2\rangle$ for all shots, where Q and γ denote electron beam total charge and Lorentz factor, respectively. A constant, $C_\gamma = 1 \times 10^5$ has been added to the normalised total counts for all shots to allow the data to be shown on a logarithmic scale. Nulls (blue, 608 shots) consist of combined misses and beam-off shots. The latter lie within 1σ (cyan, dashed) of the scaling of background gamma yield with $Q\langle\gamma^2\rangle$ (cyan, continuous), where σ is the standard deviation of the fit to the background scaling. The small fraction of nulls that lie above this threshold are beam-off shots. Hits (red, 687 shots) lie 3σ (orange, dashed) above the background scaling. The grey points cannot be categorised as

hits or nulls and thus are excluded from the analysis. The shots analysed using the Bayesian framework are encircled (black). **b** Simulated post-collision electron spectra, normalised by integration, predicted by different radiation reaction models for a collision between an electron beam (pre-collision spectrum shown) with a Gaussian temporal profile with full-width half-maxima (FWHM) 141 fs and a laser pulse with $a_0 = 14$ and Gaussian transverse and longitudinal intensity profiles with FWHM 2.47 μm and 45 fs, respectively. The collision was offset temporally from the laser focus by 60 fs. The mean energy, $\langle E \rangle$, and peak height above the 70th percentile electron energy, P_{70}, which indicates the prominence of the high-energy peak in the spectrum, are shown.

variation in electron spectra and whether any such differences are consistent with radiation reaction. Compared to the pre-collision spectrum, simulated post-collision spectra have lower mean energies, $\langle E \rangle$, and less pronounced peaks above the 70th percentile energy, P_{70}, calculated using electron spectra normalised by integration. The 70th percentile energy is the energy under which 70% of

the electron beam charge lies. Changes in P_{70} reflect the redistribution of charge due to spectral broadening. Spectral broadening may reflect stochasticity or spatial and temporal misalignments between the laser pulse and electrons, which cause equally energetic electrons to experience different laser intensities and hence energy losses.
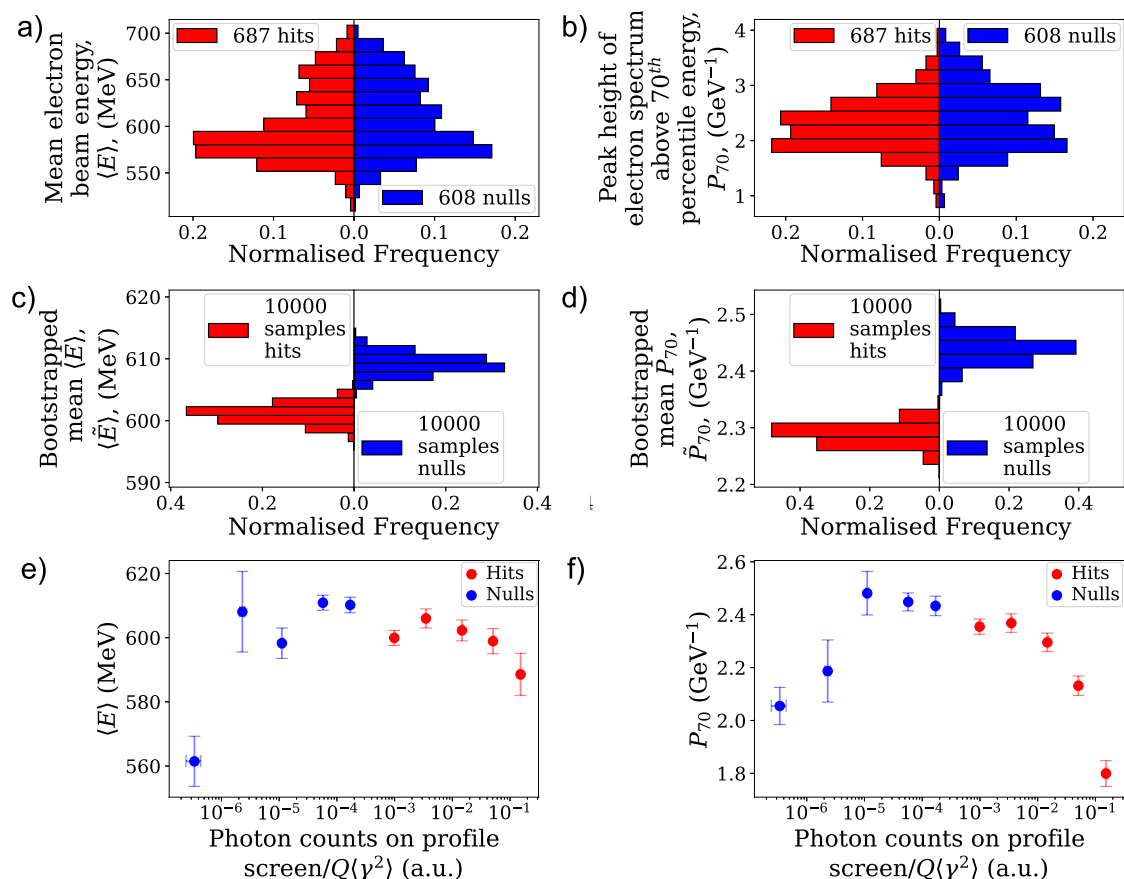
Fig. 3 | Model-independent analysis of electron energy loss and photon yield. Distributions of **a** $\langle E \rangle$ and **b** P_{70} for measured hits (red) and nulls (blue). Hit and null distributions have been normalised to the total number of shots in each. Hit and null distributions of (**c**) mean $\langle E \rangle$, denoted $\widetilde{E}$, and **d** mean P_{70}, denoted $\widetilde{P}_{70}$, obtained by bootstrapping hit and null distributions in **a**, **b** respectively. Bottom: **e** Mean $\langle E \rangle$ for the 687 hits and 607 nulls analysed, binned logarithmically by gamma profile yield normalised to $Q\langle \gamma^2 \rangle$, error bars reflect the standard error of $\langle E \rangle$ per bin; different bins contain different numbers of shots. **f** Similar to **e**, for P_{70}.

In Fig. 3a, b, there are fewer high-energy electron spectra and fewer strongly-peaked spectra for hits compared to nulls, meaning fewer high-energy and more low-energy electron beams in the former population compared to the latter. Two-sample Kolmogorov-Smirnov (KS) tests (selected for applicability to arbitrary distributions) confirm this, indicating the null hypothesis that hits and nulls originated from the same distribution can be rejected at the 5σ ($p = 5.3 \times 10^{-9}$) and 4σ ($p = 2.7 \times 10^{-5}$) levels for P_{70} and $\langle E \rangle$, respectively.

The distribution of mean values, $\widetilde{E}$, calculated for the distribution of $\langle E \rangle$ in Fig. 3a using bootstrapping (see section 'Bootstrapping') is shown in Fig. 3c. The distribution of mean values for P_{70}, denoted $\widetilde{P}_{70}$, is shown in Fig. 3b. The hit distribution means for $\widetilde{E}$ and $\widetilde{P}_{70}$ lie 3σ ($p = 2.0 \times 10^{-4}$) and 5σ ($p = 3.3 \times 10^{-7}$) below the corresponding means for nulls, respectively. The close agreement between the significance values obtained using KS tests and by bootstrapping attests to their reliability. The highly significant observation of lower mean electron energies and lower peak heights for hits compared to nulls is consistent with electron energy loss and spectral broadening and constitutes strong evidence of radiation reaction.

As illustrated in Fig. 2a, photon yields for all background sources (betatron radiation, bremsstrahlung) and thus for nulls, scale positively with $Q\langle \gamma^2 \rangle$, where Q and $\langle \gamma^2 \rangle$ denote the total charge and expected value of γ^2 for the electron beam, respectively. The photon counts in Fig. 3e, f are normalised by $Q\langle \gamma^2 \rangle$ to remove this background scaling to first-order. After this correction is applied, a small residual positive correlation remains for the nulls.

For hits in Fig. 3e, f, P_{70} and $\langle E \rangle$ decrease with increasing normalised photon yield. For the brightest hits, P_{70} and $\langle E \rangle$ lie 15σ and 7σ

below the null means, respectively. Thus, the electron beam has lower energy for successful collisions compared to unsuccessful collisions, consistent with radiation reaction.

By contrast to the positive scaling observed for nulls, hits exhibit a negative scaling with gamma yield, consistent with energy loss and hence radiation reaction. The correlation coefficients for hits and nulls differ significantly, by 40σ and 34σ for P_{70} and $\langle E \rangle$, respectively (see Supplementary Fig. 10, Supplementary Information A.3). The negative correlations observed for hits demonstrate that different physical mechanisms dominate radiation production compared to nulls and confirm that energy losses 'switch-on' for successful collisions.

The highly significant observation of electron energy loss during successful collisions, together with the strong correlation between increasing photon yield and greater electron energy loss, constitutes an observation of radiation reaction on particles.

All-optical experiments offer advantages such as natural timing and alignment of the electron beam and the colliding laser, but also present challenges. Parameters such as laser intensity and the relative size, duration and spatio-temporal overlap of the electron beam and the colliding laser pulse strongly affect post-collision electron and photon spectra, but are not measured on-shot and vary substantially between shots. This precludes the straightforward model comparison illustrated in Fig. 1b and necessitates an analysis that accounts for uncertainties due to unknown pre-collision electron spectra and unknown collision parameters when comparing radiation reaction models. This was achieved using Bayesian inference.

If a model, M, depends on parameters with unknown values, Bayesian inference estimates these parameters by constructing the
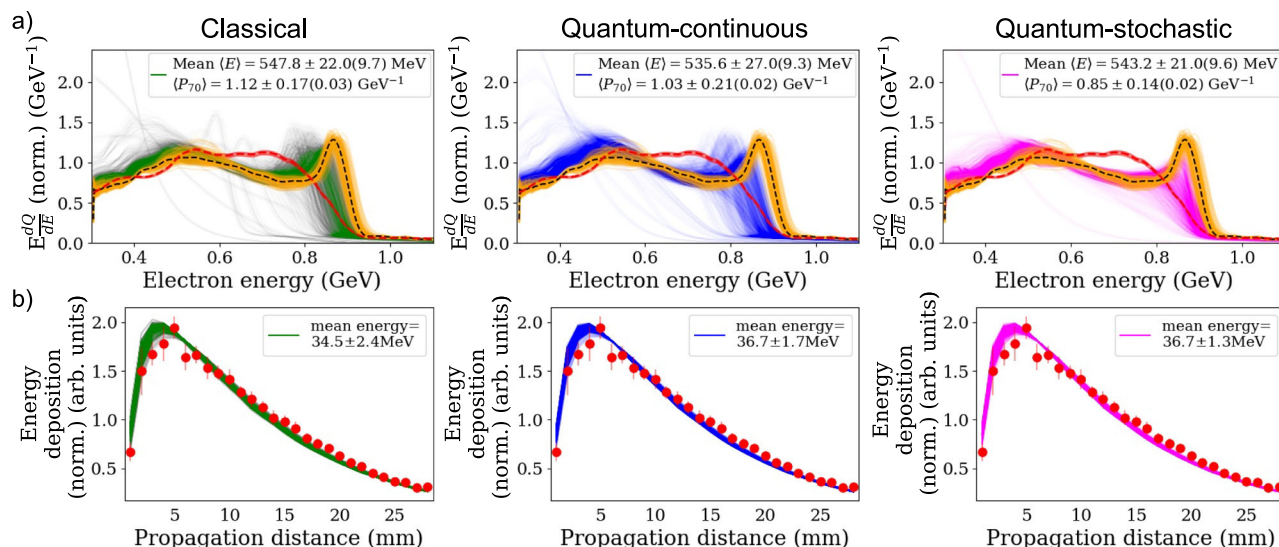
Fig. 4 | Bayesian inference results for the highest gamma-yield shot normalised to $Q\langle\gamma^2\rangle$ (shot 2). Measured data (red) and predictions for the classical (green), quantum-continuous (blue), and quantum-stochastic (magenta) models, which inferred $\langle\tilde{a}_0\rangle = 6.2 \pm 1.0$ and $\sigma_{a_0} = 1.2 \pm 0.3$, $\langle\tilde{a}_0\rangle = 6.8 \pm 0.9$ and $\sigma_{a_0} = 0.4 \pm 0.1$ and $\langle\tilde{a}_0\rangle = 6.7 \pm 0.9$ and $\sigma_{a_0} = 0.4 \pm 0.1$, respectively. **a** Measured and inferred post-collision electron spectra. The shaded region on the measured spectrum reflects the systematic error due to uncertainties in the positions of the magnet and scintillating screens. For the former, $\langle E \rangle = (564.1 \pm 0.0(10.3))$ MeV, $P_{70} = (0.83 \pm 0.00(0.01))$ GeV^{-1}. The distribution of pre-collision electron spectra predicted by the neural network (orange), for which $\langle E \rangle = (574.1 \pm 3.9(10.7))$ MeV, $P_{70} = (1.29 \pm 0.05(0.02))$ GeV^{-1} and its median (black). **b** Measured and inferred photon energy deposition in each scintillation crystal as a function of propagation distance in the CsI photon spectrometer. Error bars indicate the standard deviation of scintillation light in each crystal combined with the standard error from the photon number calibration. The mean photon energy measured was (63.3 ± 5.8) MeV.

probability that the model is accurate given the data observed, D, called the posterior probability, $P(M \mid D)$ (this notation integrates over all parameter values). The most likely parameter values are those that optimise the posterior probability.

The posterior probability is calculated using Bayes' theorem, given in Eq. (1)[57],

$$P(M|D) = \frac{P(D|M)P(M)}{P(D)} \qquad (1)$$

where the likelihood, $P(D \mid M)$, is the probability of observing the data given the model, the prior probability, $P(M)$, represents prior beliefs about the model before observing data and $P(D)$ is the (constant) probability of observing the data. In the absence of an analytic expression for the posterior, the posterior distribution is computed algorithmically by iteratively sampling model parameters, calculating the corresponding likelihood and hence updating the posterior until convergence is reached. For efficiency, high-probability regions of the parameter space are preferentially sampled.

As pre-collision electron spectra were not measured for successful collisions, distributions of pre-collision electron spectra were predicted for these shots using a neural network[58], given the measured laser energy, plasma density and longitudinal profile of plasma recombination light. The distribution variance reflects the prediction uncertainty, which, together with experimental uncertainties, is accounted for in the Bayesian analysis.

Collision parameters that could not be measured were inferred using Bayesian inference[56]. To avoid over-fitting and excessive computational run times[56], only a subset of collision parameters was inferred and all other parameters were fixed. We chose to infer τ_e, a_0 and the longitudinal displacement of the collision from the laser focus, Z_d, as they have the highest expected impact on the post-collision electron and photon spectra and exhibit degeneracies with parameters that were not inferred. Degeneracies allow different combinations of collision parameters to produce the same collision distributions of η and a_0, denoted by $\tilde{\eta}$ and $\tilde{a}_0$ and hence the same observables, as

discussed in section 'Free and fixed parameter selection, Bayesian inference test cases' and by Los et al.[56]. Hence, the inference procedure returns 'effective' values for τ_e, a_0 and Z_d; so called as they reflect the distributions of $\tilde{\eta}$ and $\tilde{a}_0$ that reproduce the observables, rather than accurately representing electron beam and laser properties.

Transverse misalignments between the electron beam and the laser pulse, r_d, were assumed to be 0. To maximise the probability that this condition was met, only the ten shots with the highest gamma yields normalised by $Q\langle\gamma^2\rangle$ were analysed. Constraints in computational resources limited the number of shots analysed; each inference required ≈19200 CPU h, 60 GB per CPU.

Three inferences were performed per shot; one for each model of radiation reaction. During each inference, different sets of collision parameters were combined with the predicted pre-collision electron spectrum to reconstruct different collisions and predict corresponding post-collision electron and photon spectra for the relevant radiation reaction model.

Although the 'true' parameters are unknown, the relative validity of two models can be compared using the ratio of model evidence or Bayes factor (see Eq. (6), section 'Analytical Methods'). The model evidence is obtained by integrating the likelihood weighted by the parameter priors over all parameter space. Bayes factors provide a more robust metric of model performance compared to a frequentist approach (e.g. a reduced chi-squared for a least-squares fit), which only compares the validity of a model to a null hypothesis for the 'best-fit' parameters.

The Bayesian analysis was tested on realistic electron spectra for various simulated collisions with differing collision parameters. For each test, the Bayesian analysis consistently favoured the correct model and inferred the first moments of the collision distributions of $\tilde{\eta}$ and $\tilde{a}_0$, respectively denoted by $\langle\tilde{\eta}\rangle$ and $\langle\tilde{a}_0\rangle$, within 1σ of their simulation values. Model differentiation was only accurate for $r_d \leq 1.6w_0$, where $w_0 = 2.5$ μm was the laser waist at focus[56].

Measured and inferred post-collision electron and photon spectra are shown in Fig. 4 for the highest normalised gamma yield shot. Additional results are provided in the Supplementary Information A.2.
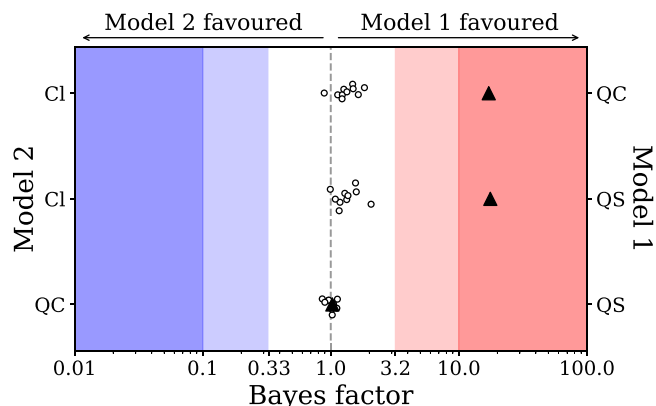
Fig. 5 | Bayesian comparison of radiation reaction models. Bayes factors for individual shots (circles) and combined over ten shots (triangles) are shown. Weak (white), substantial (light shading) and strong (dark shading) evidence favouring model 1 (red) or model 2 (blue) are categorised according to the half-log scale convention outlined by Kass and Raftery[59]. The dashed grey line indicates equal performance of the compared models.

In Fig. 4a, the $\langle E \rangle$ and P_{70} measured post-collision lie 3σ and 11σ below the neural net pre-collisionpredictions, respectively; note systematic uncertainties cancel as the correlation coefficient is 1. Only the quantum-stochastic model infers both $\langle E \rangle$ and P_{70} within 1σ of the measured spectrum, indicating marginally higher performance. Both quantum models predict more accurate photon spectra with lower uncertainties than the classical model, as indicated by the mean photon energies in Fig. 4b. Typically, the inferred photon energy deposition lies within 1σ of the measured energy deposition, confirming the goodness of fit for this diagnostic. The requirement to reproduce both electron and photon spectra using only three fitting parameters places a stronger constraint than an analysis considering a single diagnostic, which risks overfitting. This accounts for the discrepancy between measured and inferred mean photon energies and highlights the importance of considering multiple diagnostics simultaneously.

In Fig. 5, individual shots yield weak (Bayes factor < 3.2[59]) but consistent evidence favouring the quantum models over the classical model, increasing the credibility of the former. The Bayes factors for the quantum-continuous and quantum-stochastic models lie consistently around 1, signifying their comparable performance. As the inferred parameters for each shot are independent, model evidence can be combined by multiplication. The combined Bayes factors over 10 shots indicate strong evidence favouring the quantum-stochastic and quantum-continuous models over the classical model, but insufficient evidence to distinguish between the quantum models.

The quantum models better replicate both photon and electron spectra simultaneously compared to classical predictions, as they predict lower energy losses. The electron spectra largely determine the posterior location, while photon spectra predominantly affect the posterior shape as their likelihood distributions are far narrower; inferred photon spectra have fewer degrees of freedom and thus are less accurate than inferred electron spectra, but their fractional uncertainties are not substantially greater. Thus, both diagnostics play a critical role in constraining the posterior. As electron spectra contribute similarly to the posterior probability across all models, as indicated by their inferred $\langle E \rangle$ and P_{70}, relative model performance is determined by the photon spectrum. Quantum models yield higher posterior probabilities than the classical model as they infer photon spectra more accurately and with lower uncertainty. The novel ability to analyse photon and electron spectra within one self-consistent framework is critical for model comparison and a key strength of this Bayesian approach.

The quantum-stochastic model inferred $0.05 \leq \langle \tilde{\eta} \rangle \leq 0.1$ and $7 \leq \langle \tilde{a}_0 \rangle \leq 13$ across ten shots. For the inferred $\langle \tilde{a}_0 \rangle \geq 7$, the transverse offset was $r_d \leq 0.64\, w_0$, well within the range of r_d for which model selection is accurate.

Analytic classical and quantum-stochastic models[60,61] and a numerical quantum-continuous model provide an independent corroboration of the Bayesian analysis. A Gaussian is fitted to the high-energy peak in the pre-collision electron spectrum in Fig. 4a. Using the $\langle \tilde{a}_0 \rangle$ inferred by the Bayesian analysis, the corresponding post-collision spectrum is predicted analytically for each model. The mean energy, $\langle E_p \rangle$, and standard deviation, σ_p, of the pre-collision peak are $\langle E_p \rangle = 864$ MeV and $\sigma_p = 32$ MeV (4%). The post-collision peak predicted by the classical model has $\langle E_p \rangle = 807$ MeV and $\sigma_p = 19$ MeV (2%), while quantum-continuous and quantum-stochastic models predict peaks with $\langle E_p \rangle = 803$ MeV and $\sigma_p = 34$ MeV (4%) and $\langle E_p \rangle = 814$ MeV and $\sigma_p = 58$ MeV (16%), respectively, consistent with Arran et al.[62] and Yoffe et al.[63]. The predicted post-collision spectra are consistent with the measured data, validating the Bayesian analysis. The post-collision spectral widths predicted analytically appear to indicate the feasibility of model selection between all three models for these collision conditions. However, as large variations in laser intensity during the collision also cause spectral broadening, more precise knowledge of collision conditions is needed to differentiate between quantum models.

The onset of quantum effects and reduced accuracy of the Landau-Lifshitz model observed for $0.05 \leq \langle \tilde{\eta} \rangle \leq 0.1$ and $7 \leq \langle \tilde{a}_0 \rangle \leq 13$ motivate the use of quantum-corrected models in this regime. Quantum-corrected radiation reaction models predict lower energy losses for charged particles in strong fields compared to classical models, with wide-ranging consequences. Quantum-corrected ICS photon spectra have fewer high-energy photons; this has implications for ICS-based photon sources used for imaging and nuclear physics. In astrophysical environments, a quantum-corrected synchrotron emission reduces emission and cooling rates of pulsars and galactic nuclei jets and affects synchrotron emission-based estimates of magnetic field strengths. Quantum-corrected radiation models indicate higher centre-of-mass energies in particle accelerators, while for laser-solid target ion acceleration, such models predict stronger sheath fields and hence higher ion energies.

In conclusion, we report a highly significant observation of radiation reaction on electron and photon spectra and present quantitative, strong evidence to favour two quantum models over a classical model, for $0.05 \leq \langle \tilde{\eta} \rangle \leq 0.1$ and $7 \leq \langle \tilde{a}_0 \rangle \leq 13$, due to the lower energy losses the former predict. While spectral broadening was observed, insufficient knowledge of collision parameters and large uncertainties on predicted pre-collision electron spectra inhibited our ability to determine whether this arose due to stochasticity. Model differentiability would improve with stable, mono-energetic electron beams and strongly constraining priors motivated by collision parameter measurements. Lower variation in transverse alignment or in collisions with an expanded, higher-power laser would boost statistics at higher a_0, facilitating investigations of quantum phenomena over a greater range of η and providing new insight into the validity of the quantum-continuous and quantum-stochastic models in these regimes.

Methods
Experimental methods
The experiment was conducted using the dual-beam Gemini laser at the Central Laser Facility, Rutherford Appleton Laboratory, UK. An $f/40$ off-axis parabola was used to focus one arm of the linearly polarised, two-beam system to a transverse full-width half-maximum (FWHM) of the focal spot intensity of $(35 \pm 3)\,\mu m \times (40.6 \pm 1.2)\,\mu m$. An off-shot Grenouille measurement of the FWHM duration of the laser intensity yielded (59.5 ± 2.5) fs. The laser delivered (6.8 ± 0.6) J to the target, corresponding to an $a_0 = 1.0 \pm 0.15$ (standard deviation given).

The laser-wakefield drive beam was focused into a 15 mm supersonic gas jet with a trapezoidal density profile and 5 mm ramps. An average electron density of $\approx(1.1 \pm 0.2) \times 10^{18}\,cm^{-18}$ was attained at the peak of the trapezoidal profile with He gas, doped with 1% N_2 to induce ionisation injection[64].

The electron beam and photons produced by ICS propagated through the hole in the $f/2$ parabola, which had an acceptance angle of 42 mrad. A $\int B(x)\,dx = 0.4$ T m dipole magnet was used to disperse the electron beam through a wire array onto two sequential LANEX screens, which were imaged by two cooled 16-bit cameras. The electron spectrum was subsequently retrieved with the aid of a tracking algorithm, which computed the trajectories of electrons through the magnetic field. The wire array and two screens allowed the degeneracy between the electron beam energy and pointing into the magnet to be de-convolved[65–67]. The systematic uncertainty in the retrieved electron energy due to the uncertainties in the relative positions of the magnet, lanex screens and gas jet was

$$\zeta_e\,[MeV] = C_e E\,[MeV]^2, \tag{2}$$

where E denotes electron energy and $C_e = 32.45 \times 10^{-6}\,MeV^{-1}$.

The wakefield accelerator produced (140 ± 1) pC electron beams with mean and standard deviation energy $(609 \pm 2(stat)(12)(syst))$ MeV and shot-to-shot standard deviation (40 ± 1) MeV, respectively (standard error given). Electrons with energies < 300 MeV could not be measured. A radial source size of < (0.7 ± 0.1) μm was assumed, in line with previous measurements[68,69]. The FWHM energy-dependent electron beam divergence, θ_D, measured along the axis transverse to the dispersion plane by the LANEX screens, which measured the electron spectrum, was $(b_1 - b_2\sqrt{\gamma m_e\,[GeV]})$, where $b_1 = 1.30^{+0.26}_{-0.19}$ mrad, $b_2 = 0.26^{+0.24}_{-0.28}$ mrad $GeV^{-0.5}$. The axial symmetry of the electron beam divergence was confirmed using linear Thomson scattering[70].

The colliding laser pulse was focused at the rear of the gas jet by an $f/2$ parabola with a 25.4 mm on-axis hole. The laser intensity profile had transverse FWHM (2.5 ± 0.2) μm × (2.1 ± 0.1) μm and FWHM duration (45.0 ± 2.5) fs. Due to energy losses in the laser system, including the on-axis hole in the $f/2$ parabola, the energy on-target was (6.13 ± 0.02) J, yielding a peak $a_0 = 21.4 \pm 1.8$.

Spatial and temporal overlap of laser pulses

Accessing collision $a_0 \gtrsim 10$ required $\lesssim 1\,μm$ and $\lesssim 10\,fs$ precision spatio-temporal overlap of the electron beam and laser focus. This required a careful alignment procedure, detailed below.

A micron knife-edge 90° prism, imaged using a × 10 microscope objective, was used to overlap the two laser pulses spatially and temporally, where the latter was achieved using spatial interferometry, as demonstrated previously[44,71]. By optimising the contrast of the interference pattern, the two laser pulses were synchronised to within ± 10 fs. To time the colliding pulse, two additional effects needed to be corrected for, namely the reduced non-linear group velocity of the wakefield-driver laser pulse in the plasma and the longitudinal displacement of the electron beam from the wakefield driver by N plasma wavelengths, where $N = \frac{1}{2}$ for an electron beam travelling at the dephasing limit with velocity close to c. Thus, the longitudinal collision position was shifted closer to the gas jet by δ_z,

$$\delta_z = \frac{3d}{4}\frac{n_e}{n_c} + N\frac{\lambda_L}{2}\sqrt{\frac{n_c}{n_e}} \tag{3}$$

where n_e and $n_c = \frac{\epsilon_0 m_e \omega_L^2}{e^2}$ are the plasma and critical densities and d is the distance from the upstream edge of the plasma to the injection point.

Fluctuations in ambient temperature altered the temporal and spatial alignment between the electron beam and the colliding laser over the course of shooting. Thus, implementing timing and pointing stabilisation was key to obtaining a high number of successful collisions.

Once timed and aligned, references for optimal timing and alignment were taken using a spectral interferometer in the laser area and a diagnostic of the $f/40$ beam pointing, respectively. Long-term drifts in spatial and temporal alignment could be corrected for by adjusting the tip and tilt of a mirror in the $f/40$ beamline and by altering the path length of one of the laser arms, respectively.

Long term timing and pointing drifts were corrected using an automated feedback loop. Thus, the remaining misalignment between the electron beam and the colliding laser resulted from shot-to-shot variation in the beam paths and the laser pointing due to vibrations. The temporal jitter between the two laser arms was assumed to be normally distributed with a standard deviation ± 30 fs. An additional source of uncertainty in the timing between the electron beam and colliding laser stems from the unknown value of d, which we assume to be uniformly distributed with lower and upper bounds of 0 mm and 10 mm, respectively. To correct for δ_z, the path between the two beams was reduced by 20 fs. Thus, the offset in timing between the two beams, $\Delta t \approx \frac{\delta_z}{c}$, 2.7 fs ≤ Δt ≤ 45.8 fs. The standard deviations of the radial positions of the colliding laser and the electron beam due to pointing variations were measured to be (0.53 ± 0.26) μm and (17.5 ± 0.5) μm, respectively, which correspond to a standard deviation in transverse alignment of (17.5 ± 0.6) μm.

Gamma radiation diagnostics

The angular distribution of gamma radiation was measured using a 50 × 50 × 10 mm profile screen consisting of 1 × 1 × 10 mm CsI(Tl) crystals separated by 0.2 mm titanium oxide spacers. Dimensions have the format (horizontal × vertical × depth). The front of the profile screen was coated with 0.5 mm titanium oxide. The profile screen was placed outside the vacuum chamber, (2244 ± 4) mm from the interaction and was imaged using a cooled 16-bit CCD camera.

The energy deposition of gamma photons was measured using a 50 × 50 × 150 mm dual-axis CsI(Tl) scintillator, comprised of alternating layers of horizontally and vertically oriented 5 × 5 × 50 mm CsI(Tl) crystals, which were held in place by a 3D printed 1 mm nylon frame and separated by 1 mm rubber spacers to prevent light leakage between crystals. Two cooled 16-bit CCD cameras imaged the scintillation light from above and laterally. The calorimeter was placed outside the vacuum chamber, (3570 ± 3) mm from the interaction.

Geant4[72,73] simulations were used to obtain the energy deposition in the CsI photon diagnostics[70] as a function of incident photon energy, as demonstrated in Behm et al.[74]. The maximum and minimum photon energies used to calculate energy deposition were 0.01 MeV and 1 GeV, respectively. These simulations included the chamber geometry, large objects inside the chamber such as the dipole magnets and all materials placed in the beam path, including a 1 mm alumina laser block, a 25 μm Kapton window with a 375 μm Kevlar backing sheet and a 25 μm aluminium foil. Variations in the scintillation efficiency of the crystals and in the efficiency of the imaging system were characterised and subsequently compensated for by comparing the measured and simulated response of the calorimeter to bremsstrahlung generated by an electron beam propagating through a (1.5 ± 0.1) mm PTFE target with radiation length much less than the radiation length of a 1 GeV electron beam.

The ICS spectrum, S_{ICS}, has the characteristic shape

$$S_{ICS} = A\left(\frac{E_\gamma}{E_{\gamma c}}\right)^{-\frac{2}{3}} e^{-\left(\frac{E_\gamma}{E_{\gamma c}}\right)} \tag{4}$$

where A and $E_{\gamma c}$ represent photon number and the critical energy of the spectrum, respectively. Bayesian inference was used to obtain the

values of A and $E_{\gamma c}$ for which the energy deposition calculated using Eq. (4) fitted the measured energy deposition.

Methods for frequentist analysis

Following the approach employed by Cole et al.[44], the photon yield measured by the gamma profile diagnostic was used to identify hits and nulls. The total yield measured by the profile screen, Y_γ, is expected to scale with the electron beam total charge, Q and expected value of γ^2, $\langle\gamma^2\rangle$:

$$Y_\gamma = (C_{ICS}a_0^2 + C_{BKG})Q\langle\gamma^2\rangle \qquad (5)$$

where the first and second terms describe the contributions of ICS and background (e.g. due to bremsstrahlung) to the total yield, respectively and C_{ICS}, C_{BKG}, are scaling constants. The scaling for ICS with photon yield holds for $\gamma a_0^2 < 5.5 \times 10^5$[75]. Multiple sets of shots in which the counter-propagating laser was not fired were taken to obtain the characteristic background scaling with $Q\langle\gamma^2\rangle$. Misses and hits, classified as shots which produced yields within 1σ and above 3σ of the background scaling, respectively, are shown in Fig. 2.

In this work, we present a controlled experiment in which the only difference between hits and nulls is the presence or absence of a collision between a laser and an electron beam, respectively. Systematic changes in electron beam properties and the effect of background radiation mechanisms were mitigated and accounted for, if necessary.

Long-term drifts in the laser pointing and timing, which could produce systematic changes in the electron spectra and overlap of the electron beam and laser at the collision, were minimised using automated correction of the spatial and temporal overlap of the wakefield drive laser and the colliding laser. Hits and nulls were interleaved to ensure null electron beams were representative of hits.

Background radiation mechanisms, namely betatron and bremsstrahlung, were characterised using laser-off shots. Distributions of the mean electron beam energy, $\langle E\rangle$, and height of its spectral peak above the 70th percentile energy, P_{70}, were obtained for hits and nulls. Both background radiation mechanisms produce a positive scaling between photon yield and $Q\langle\gamma^2\rangle$.

All radiation reaction models predict a reduction in $\langle E\rangle$ and P_{70} (the latter is predicted for all models if the electron beam interacts with a range of laser intensities), for hits compared to nulls and a photon yield which increases with decreasing P_{70} and decreasing $\langle E\rangle$. These model-independent metrics of radiation reaction were compared for hits and nulls.

No known systematic background effect can produce the reduction in $\langle E\rangle$ and P_{70} for successful collisions and the negative scaling of $\langle E\rangle$ and P_{70} with photon yield simultaneously. Background radiation sources produce a positive scaling of photon yield with $Q\langle\gamma^2\rangle$, opposite to the trend predicted for radiation reaction. As hits and nulls were interleaved, both systematic and random changes in laser and electron properties would affect both hits and nulls equally, in contrast to radiation reaction models' predictions.

Given that the only difference between hits and nulls is the presence or absence of a collision between the electron beam and laser, the simultaneous observation of all of the above signatures of radiation reaction signatures for hits and their absence for nulls constitutes a definitive observation of radiation reaction.

Analytical methods

Free and fixed parameter selection, Bayesian inference test cases. A full, detailed account of the implementation and testing of the Bayesian inference framework and the forward models used therein is provided in ref. 56.

Several parameters (including electron beam source size and chirp, laser duration, transverse offset, etc) have been assigned fixed values in the forward model (i.e. are not inferred). Free and fixed parameters were chosen in accordance with the following criteria:

- The expected effect of variation. This incorporates both the probability of parameter variation by a given amount and the impact of this variation on the post-collision electron and photon spectra. Parameters fixed due to their small expected effect include laser duration and focal spot size and electron beam chirp.
- Shot selection. The ten shots which produced the highest CsI profile screen yields, normalised to $Q\langle\gamma^2\rangle$, were analysed using the Bayesian framework. As the laser intensity decreases most steeply with transverse (rather than longitudinal) misalignment, by analysing the highest yield shots the probability of a large transverse offset is reduced.
- Degeneracy. If changes in two (or more) collision parameters engender similar alterations in post-collision observables, it is possible to fix one of these parameters and vary the second to reproduce the effect of the fixed parameter. For example, if the electron beam has finite divergence, varying the longitudinal position of the collision alters the size of the electron beam at the collision. This produces post-collision observables similar to those obtained by varying the electron beam source size. Degeneracy allows changes in the electron beam source size, divergence and transverse offset from the laser focus to be compensated by free parameters (laser energy, longitudinal offset of the collision from focus, electron beam duration). The laser energy was chosen as a free parameter to enable the Bayesian inference procedure to tackle shot-to-shot variations therein.

The laser, electron and collision parameters which were measured, estimated or inferred based on previous measurements, are summarised alongside their assigned values in the forward models in Supplementary Table 1, Supplementary Table 2 and Supplementary Table 3, respectively, in the Supplementary Information A.1.

Bayesian inference implementation and testing. The Bayesian inference procedures used the Markov chain Monte Carlo[76] from the Python package emcee. Lack of on-shot parameter measurements necessitated broad priors[56].

Extensive testing of the Bayesian analysis[56], which included inferences on synthetic data where the fixed collision parameters (e.g. Z_d) were assigned different values from the forward models, revealed that for all test cases the inference procedure yielded weak evidence favouring the correct model; none of the test cases yielded false positives. This is a clear demonstration of the accuracy of the model selection capabilities of the Bayesian framework we have developed. In all test cases, the highest performing model(s) inferred $\langle\tilde{a}_0\rangle$ and $\langle\eta\rangle$ within 1σ of the input (correct) value. This shows the analysis infers the physical parameters governing the collision accurately to first order, in spite of the simplifying assumptions made.

Bayes factors. The Bayes factor, P_X/P_Y, for models X and Y, used to perform model comparison, is defined as the integral over the marginalised posterior/likelihood

$$\frac{P_X}{P_Y} = \frac{\int p(\phi_X|M_X)p(D|\phi_X, M_X)d\phi_X}{\int p(\phi_Y|M_Y)p(D|\phi_Y, M_Y)d\phi_Y} \qquad (6)$$

where, ϕ_X, ϕ_Y are the parameter vectors which characterise models M_X and M_Y, respectively. The integrals in Eq. (6) do not have analytic solutions and are challenging to compute numerically due to the complex shape of the posterior distribution. Therefore, the Bayes factor was approximated using leave-one-out cross-validation with Pareto-smoothed importance sampling (LOO-PSIS)[77] available from the Python package arviz[78]. As the inferred parameters and hence the

posterior probabilities for each shot are independent, their product yields the total Bayes factor.

Bootstrapping. Bootstrapping, chosen for its applicability to non-normal distributions, was used to compute the errors on population means of the hit and null distributions for $\langle E \rangle$ and P_{70}, shown in Fig. 3. Bootstrapping was also used to compute the mean and standard error for the null scaling of photon counts measured by the profile screen with $Q\langle \gamma^2 \rangle$, illustrated in Fig. 2. In each instance where bootstrapping was employed in the analysis, a sample size equal to that of the dataset was used and the data was re-sampled 10,000 times. The robustness of the bootstrapping analysis was verified by increasing the number of re-samples by a factor of 100, which did not significantly affect the results. The random randint package from the numpy library in Python was used to perform sampling.

Data availability
The authors declare that all processed data supporting the findings of this study are available on Code Ocean at https://doi.org/10.24433/CO.7757204.v1 or within the article and its Supplementary Information files. Raw data may be obtained from the corresponding author upon request.

Code availability
The authors declare that all code supporting the findings of this study is available on Code Ocean at https://doi.org/10.24433/CO.7757204.v1.

References
1. Fedotov, A. et al. Advances in QED with intense background fields. *Phys. Rep.* **1010**, 1–138 (2023).
2. Di Piazza, A., Müller, C., Hatsagortsyan, K. Z. & Keitel, C. H. Extremely high-intensity laser interactions with fundamental quantum systems. *Rev. Mod. Phys.* **84**, 1177–1228 (2012).
3. Ritus, V. I. Quantum effects of the interaction of elementary particles with an intense electromagnetic field. *J. Sov. Laser Res.* **6**, 497–617 (1985).
4. Timokhin, A. N. Time-dependent pair cascades in magnetospheres of neutron stars – I. Dynamics of the polar cap cascade with no particle supply from the neutron star surface. *Mon. Not. R. Astron. Soc.* **408**, 2092–2114 (2010).
5. Willingale, L. et al. Status of the ZEUS laser user facility. In *CLEO 2023*, SM1D.7 (Optica Publishing Group, 2023). https://opg.optica.org/abstract.cfm?URI=CLEO_SI-2023-SM1D.7.
6. Doria, D. et al. Overview of Eli-np status and laser commissioning experiments with 1-pW and 10-pW class lasers. *J. Instrum.* **15**, C09053 (2020).
7. Gan, Z. et al. *The Shanghai Superintense Ultrafast Laser Facility (SULF) Project*, 199–217 (Springer International Publishing, 2021).
8. Matheron, A. et al. Probing strong-field QED in beam-plasma collisions. *Commun. Phys.* **6**, 141 (2023).
9. Wistisen, T. N., Di Piazza, A., Knudsen, H. V. & Uggerhøj, U. I. Experimental evidence of quantum radiation reaction in aligned crystals. *Nat. Commun.* **9**, 795 (2018).
10. Yakimenko, V. et al. Prospect of studying nonperturbative QED with beam-beam collisions. *Phys. Rev. Lett.* **122**, 190404 (2019).
11. Harding, G. & Harding, E. Compton scatter imaging: a tool for historical exploration. *Appl. Radiat. Isot.* **68**, 993–1005 (2010).
12. Placidi, M., Di Mitri, S., Pellegrini, C. & Penn, G. Compact fel-driven inverse Compton scattering gamma-ray source. *Nucl. Instrum. Methods Phys. Res. A Accel. Spectrom. Detect. Assoc. Equip* **855**, 55–60 (2017).
13. Tashima, H. & Yamaya, T. Compton imaging for medical applications. *Radiol. Phys. Technol.* **15**, 187–205 (2022).
14. Albert, F. et al. Design of narrow-band Compton scattering sources for nuclear resonance fluorescence. *Phys. Rev. Spec. Top. Accel. Beams* **14**, 050703– (2011).
15. Geddes, C. G. R. et al. Compact quasi-monoenergetic photon sources from laser-plasma accelerators for nuclear detection and characterization. *Nucl. Instrum. Methods Phys. Res. Sect. B Beam Interact. Mater. At.* **350**, 116–121 (2015).
16. Gibson, D. J. et al. Design and operation of a tunable MeV-level Compton-scattering-based γ-ray source. *Phys. Rev. Spec. Top. Accel. Beams* **13**, 070703– (2010).
17. Telnov, V. I. Gamma-gamma collider with wγγ≤12 GeV based on the 17.5 Gev sc Linac of the European XFEL. *J. Instrum.* **15**, P10028 (2020).
18. Landau, L. D. & Lifshitz, E. M. *The Classical Theory of Fields* 3rd edn, Vol. 2 (Pergammon Press, 1971).
19. Baier, V. N., Katkov, V. M. & Strakhovenko, V. M. *Electromagnetic Processes at High Energies in Oriented Single Crystals* (World Scientific, 1998).
20. Gonoskov, A., Blackburn, T. G., Marklund, M. & Bulanov, S. S. Charged particle motion and radiation in strong electromagnetic fields. *Rev. Mod. Phys.* **94**, 045001 (2022).
21. Di Piazza, A., Hatsagortsyan, K. Z. & Keitel, C. H. Quantum radiation reaction effects inmultiphoton Compton scattering. *Phys. Rev. Lett.* **105**, 220403 (2010).
22. Philippov, A. A. & Spitkovsky, A. Ab-initio pulsar magnetosphere: particle acceleration in oblique rotators and high-energy emission modeling. *Astrophys. J.* **855**, 94 (2018).
23. Lyubarskii, Y. E. A model for the energetic emission from pulsars. *Astron. Astrophys.* **311**, 172–178 (1996).
24. Uzdensky, D. A. & Spitkovsky, A. Physical conditions in the reconnection layer in pulsar magnetospheres. *Astrophy. J.* **780**, 3 (2013).
25. Sultana, J., Kazanas, D. & Mastichiadis, A. The supercritical pile gamma-ray burst model: the GRB afterglow steep decline and plateau phase. *Astrophys. J.* **779**, 16 (2013).
26. Zhang, P., Bulanov, S. S., Seipt, D., Arefiev, A. V. & Thomas, A. G. R. Relativistic plasma physics in supercritical fields. *Phys. Plasmas* **27**, 050601 (2020).
27. Jaroschek, C. H. & Hoshino, M. Radiation-dominated relativistic current sheets. *Phys. Rev. Lett.* **103**, 075002 (2009).
28. Weber, S. et al. P3: An installation for high-energy density plasma physics and ultra-high intensity laser–matter interaction at ELI-Beamlines. *Matter Radiat. Extrem.* **2**, 149–176 (2017).
29. Zou, J. P. et al. Design and current progress of the Apollon 10 PW project. *High. Power Laser Sci. Eng.* **3**, e2 (2015).
30. Borghesi, M. et al. Fast ion generation by high-intensity laser irradiation of solid targets and applications. *Fusion Sci. Technol.* **49**, 412–439 (2006).
31. Tajima, T., Yan, X. Q. & Ebisuzaki, T. Wakefield acceleration. *Rev. Mod. Plasma Phys.* **4**, 7 (2020).
32. Albert, F. & Thomas, A. G. R. Applications of laser wakefield accelerator-based light sources. *Plasma Phys. Control. Fusion* **58**, 103001 (2016).
33. Compton, A. H. A quantum theory of the scattering of x-rays by light elements. *Phys. Rev.* **21**, 483–502 (1923).
34. Nakamura, T. et al. High-power γ-ray flash generation in ultraintense laser-plasma interactions. *Phys. Rev. Lett.* **108**, 195001 (2012).
35. Zhidkov, A., Koga, J., Sasaki, A. & Uesaka, M. Radiation damping effects on the interaction of ultraintense laser pulses with an overdense plasma. *Phys. Rev. Lett.* **88**, 185002 (2002).
36. Capdessus, R. & McKenna, P. Influence of radiation reaction force on ultraintense laser-driven ion acceleration. *Phys. Rev. E* **91**, 053105 (2015).
37. Salgado, F. C. et al. Single particle detection system for strong-field QED experiments. *New J. Phys.* **24**, 015002 (2022).

38. Abramowicz, H. et al. Conceptual design report for the luxe experiment. *Eur. Phys. J. Spec. Top.* **230**, 2445–2560 (2021).

39. Blackburn, T. G. Radiation reaction in electron–beam interactions with high-intensity lasers. *Rev. Mod. Plasma Phys.* **4**, 5 (2020).

40. Blackburn, T. G., Ridgers, C. P., Kirk, J. G. & Bell, A. R. Quantum radiation reaction in laser–electron-beam collisions. *Phys. Rev. Lett.* **112**, 015001 (2014).

41. Kirk, J. G., Bell, A. R. & Arka, I. Pair production in counter-propagating laser beams. *Plasma Phys. Control. Fusion* **51**, 085008 (2009).

42. Ridgers, C. P. et al. Signatures of quantum effects on radiation reaction in laser–electron-beam collisions. *J. Plasma Phys.* **83**, 715830502 (2017).

43. Poder, K. et al. Experimental signatures of the quantum nature of radiation reaction in the field of an ultraintense laser. *Phys. Rev. X* **8**, 031004 (2018).

44. Cole, J. M. et al. Experimental evidence of radiation reaction in the collision of a high-intensity laser pulse with a laser-wakefield accelerated electron beam. *Phys. Rev. X* **8**, 011020–1 (2018).

45. Mirzaie, M. et al. All-optical nonlinear Compton scattering performed with a multi-petawatt laser. *Nat. Photonics* **18**, 1212–1217 (2024).

46. Matheron, A. et al. Compton photons at the GeV scale from self-aligned collisions with a plasma mirror. Preprint at https://arxiv.org/abs/2412.19337 (2024).

47. Bula, C. et al. Observation of nonlinear effects in Compton scattering. *Phys. Rev. Lett.* **76**, 3116–3119 (1996).

48. Burke, D. L. et al. Positron production in multiphoton light-by-light scattering. *Phys. Rev. Lett.* **79**, 1626–1629 (1997).

49. Bamber, C. et al. Studies of nonlinear QED in collisions of 46.6 GeV electrons with intense laser pulses. *Phys. Rev. D.* **60**, 092004 (1999).

50. Sands, M. Observation of quantum effects in an electron synchrotron. *IlNuovo Cimento.* **15**, 599–605 (1960).

51. Wistisen, T. N., Di Piazza, A., Nielsen, C. F., Sørensen, A. H. & Uggerhøj, U. I. Quantum radiation reaction in aligned crystals beyond the local constant field approximation. *Phys. Rev. Res.* **1**, 033014 (2019).

52. Nielsen, C. F., Justesen, J. B., Sørensen, A. H., Uggerhøj, U. I. & Holtzapple, R. Radiation reaction near the classical limit in aligned crystals. *Phys. Rev. D.* **102**, 052004 (2020).

53. Neitz, N. & Di Piazza, A. Stochasticity effects in quantum radiation reaction. *Phys. Rev. Lett.* **111**, 054802 (2013).

54. Niel, F., Riconda, C., Amiranoff, F., Duclous, R. & Grech, M. From quantum to classical modeling of radiation reaction: a focus on stochasticity effects. *Phys. Rev. E* **97**, 043209 (2018).

55. Los, E. Experimental studies of radiation reaction in strong fields with Bayesian inference and model selection. http://hdl.handle.net/10044/1/107161 (2023).

56. Los, E. E. et al. A Bayesian framework to investigate radiation reaction in strong fields. *High. Power Laser Sci. Eng.* **13**, e25 (2025).

57. Heard, N. *Uncertainty and Decisions* 1–14 (Springer International Publishing, 2021). https://doi.org/10.1007/978-3-030-82808-0_1.

58. Streeter, M. J. V. et al. Laser wakefield accelerator modelling with variational neural networks. *High. Power Laser Sci. Eng.* **11**, e9 (2023).

59. Kass, R. E. & Raftery, A. E. Bayes factors. *J. Am. Stat. Assoc.* **90**, 773–795 (1995).

60. Blackburn, T. G. Analytical solutions for quantum radiation reaction in high-intensity lasers. *Phys. Rev. A* **109**, 022234 (2024).

61. Vranic, M., Grismayer, T., Fonseca, R. A. & Silva, L. O. Quantum radiation reaction in head-on laser-electron beam interaction. *New J. Phys.* **18**, 073035 (2016).

62. Arran, C. et al. Optimal parameters for radiation reaction experiments. *Plasma Phys. Control. Fusion* **61**, 074009 (2019).

63. Yoffe, S. R., Kravets, Y., Noble, A. & Jaroszynski, D. A. Longitudinal and transverse cooling of relativistic electron beams in intense laser pulses. *New J. Phys.* **17**, 053025 (2015).

64. McGuffey, C. et al. Ionization-induced trapping in a laser wakefield accelerator. *Phys. Rev. Lett.* **104**, 025004 (2010).

65. Clayton, C. E. et al. Self-guided laser wakefield acceleration beyond 1 GeV using ionization-induced injection. *Phys. Rev. Lett.* **105**, 105003 (2010).

66. Wang, X. et al. Quasi-monoenergetic laser-plasma acceleration of electrons to 2 GeV. *Nat. Commun.* **4**, 1988 (2013).

67. Soloviev, A. A. et al. Two-screen single-shot electron spectrometer for laser wakefield accelerated electron beams. *Rev. Sci. Instrum.* **82**, 043304 (2011).

68. Kneip, S. et al. X-ray phase contrast imaging of biological specimens with femtosecond pulses of betatron radiation from a compact laser plasma wakefield accelerator. *Appl. Phys. Lett.* **99**, 093701 (2011).

69. Schnell, M. et al. Deducing the electron-beam diameter in a laser-plasma accelerator using X-ray betatron radiation. *Phys. Rev. Lett.* **108**, 075001 (2012).

70. Gerstmayr, E. *Energetic Radiation from Wakefield Acceleration and its Applications. Ph.D. thesis, Imperial College London* (2020).

71. Corvan, D. J. et al. Optical measurement of the temporal delay between two ultra-short and focused laser pluses. *Opt. Express* **24**, 3127–3136 (2016).

72. Allison, J. et al. Recent developments in Geant4. *Nucl. Instrum. Methods Phys. Res. Sect. A Accel. Spectrom. Detect. Assoc. Equip.* **835**, 186–225 (2016).

73. Agostinelli, S. et al. Geant4—a simulation toolkit. *Nucl. Instrum. Methods Phys. Res. Sect. A Accel. Spectrom. Detect. Assoc. Equip.* **506**, 250–303 (2003).

74. Behm, K. T. et al. A spectrometer for ultrashort gamma-ray pulses with photon energies greater than 10 MeV. *Rev. Sci. Instrum.* **89**, 113303 (2018).

75. Thomas, A. G. R., Ridgers, C. P., Bulanov, S. S., Griffin, B. J. & Mangles, S. P. D. Strong radiation-damping effects in a gamma-ray source generated by the interaction of a high-intensity laser with a wakefield-accelerated electron beam. *Phys. Rev. X* **2**, 041004 (2012).

76. Brooks, S., Gelman, A., Jones, G. & Meng, X.-L. *Handbook of Markov Chain Monte Carlo* (CRC Press LLC, 2011). http://ebookcentral.proquest.com/lib/imperial/detail.action?docID=762505.

77. Vehtari, A., Gelman, A. & Gabry, J. Practical Bayesian model evaluation using leave-one-out cross-validation and WAIC. *Stat. Comput.* **27**, 1413–1432 (2017).

78. Kumar, R., Carroll, C., Hartikainen, A. & Martin, O. ArviZ a unified library for exploratory analysis of Bayesian models in Python. *J. Open Source Softw.* **4**, 1143 (2019).

Acknowledgements

Author contributions

A.I., A.D.P., M.T., T.G.B., C.K., M.M., E.E.L., C.A., E.G., M.J.V.S., C. Colgan, B.K., P.M., C.D.M., Z.N., C.P.R., G.S., A.G.R.T., M.Z. and S.P.D.M. conceived the study; E.E.L., C.A., E.G., M.J.V.S., C. Colgan, B.K., C.P.R., G.S. and S.P.D.M. developed the methodology; E.E.L., C.A., E.G., M.J.V.S., S.J.D.D. and P.P. developed the software; E.E.L., C.A., E.G., M.J.V.S., C. Cobo, J.C., R.F. and J.W. performed the formal analysis; E.E.L., M.T. and C.A. validated the analysis; E.E.L., C.A., E.G., M.J.V.S., C. Colgan, C. Cobo, B.K., N.B., L.C. and N.C. conducted the investigation; N.B., P.P.R., D.R.S., Z.N., C.P.R., G.S., S.P.D.M. and M.Z. provided essential resources; E.E.L., C.A., E.G. and M.J.V.S. curated the data; E.E.L. wrote the original draft; A.I., A.D.P., M.T., T.G.B., C.K., M.M., E.E.L., C.A., E.G., M.J.V.S., C. Colgan, B.K., P.M., C.P.R., G.S., A.G.R.T. and S.P.D.M. contributed to writing: review and editing; E.E.L., M.J.V.S. and S.P.D.M. prepared the visualisations; P.M., C.D.M., Z.N., C.P.R., G.S., A.G.R.T. and S.P.D.M. supervised the study; E.E.L., C.A., E.G., C. Colgan., N.B., S.J.D.D., P.P.R., C.P.R., G.S., D.R.S. and S.P.D.M. managed the project administration; C.P.R., G.S., S.P.D.M., A.G.R.T. and C.A. acquired the funding.

Competing interests

The authors declare no competing interests.

Additional information

Supplementary information The online version contains supplementary material available at https://doi.org/10.1038/s41467-025-67918-8.

Correspondence and requests for materials should be addressed to Eva E. Los.

Peer review information *Nature Communications* thanks the anonymous reviewer(s) for their contribution to the peer review of this work. A peer review file is available.

Reprints and permissions information is available at http://www.nature.com/reprints

Publisher's note Springer Nature remains neutral with regard to jurisdictional claims in published maps and institutional affiliations.

[1]The John Adams Institute for Accelerator Science, Imperial College London, London, UK. [2]School of Mathematics and Physics, Queen's University Belfast, Belfast, UK. [3]Stanford PULSE Institute, SLAC National Accelerator Laboratory, Menlo Park, CA, USA. [4]York Plasma Institute, School of Physics, Engineering and Technology, University of York, York, UK. [5]Tokamak Energy Ltd, Milton Park, Milton, UK. [6]Department of Physics, University of Gothenburg, Gothenburg, Sweden. [7]Central Laser Facility, STFC Rutherford Appleton Laboratory, Didcot, UK. [8]Gérard Mourou Center for Ultrafast Optical Science, University of Michigan, Ann Arbor, MI, USA. [9]Department of Physics and Astronomy, University of Rochester, Rochester, NY, USA. [10]Laboratory for Laser Energetics, University of Rochester, Rochester, NY, USA. [11]Max Planck Institute for Nuclear Physics, Heidelberg, Germany. [12]Higgs Centre, University of Edinburgh, Edinburgh, UK. [13]Department of Physics, Chalmers University of Technology, Gothenburg, SE, Sweden. [14]Department of Physics, SUPA, University of Strathclyde, Glasgow, UK. [15]Deutsches Elektronen-Synchrotron DESY, Hamburg, Germany. [16]Institute of Optics and Quantum Electronics, Friedrich Schiller Universität Jena, Jena, Germany. [17]Helmholtz Institute Jena, Jena, Germany. [18]GSi GmbH, Darmstadt, Germany. ✉e-mail: e.los18@imperial.ac.uk